Solar RRL
www.solar-rrl.com

High-Efficiency Nonfullerene Organic Solar Cells Enabled by Atomic Layer Deposited Zirconium-Doped Zinc Oxide

Geedhika K. Poduval, Leiping Duan, Md. Anower Hossain, Borong Sang, Yu Zhang, Yingping Zou, Ashraf Uddin,* and Bram Hoex**

Organic solar cells (OSCs) are promising photovoltaic devices and zinc oxide (ZnO) is a commonly used electron transport layer (ETL) in OSCs. However, the conventional spin-coating ZnO layer is currently limiting its efficiency potential. Herein, it is shown for the first time that atomic layer deposition (ALD), which allows for controlled thin film growth with atomic-scale control, can effectively be used to optimize the ZnO for nonfullerene OSCs. First, density functional theory (DFT) calculations are discussed to show the impact of doping ZnO with zirconium (Zr) on its density of states and detail the synthesis of Zr doped ZnO films by ALD using a supercycle approach. A 2.4% Zr concentration is found to be optimal in terms of optoelectronic properties and sufficiently low defect density. The champion efficiency of 14.7% for a PM6:N3-based nonfullerene OSC with Zr-doped ZnO ETL are obtained, which is ≈1% absolute higher compared to a device with an undoped ZnO ETL. This improvement is attributed to a lower series resistance, a suppressed surface recombination, and an enhanced current extraction resulting from the Zr-doped ZnO. This work demonstrates the potential of atomic-scale engineering afforded by ALD towards achieving the ultimate efficiency of OSCs.

1. Introduction

Organic solar cells (OSCs) have received considerable attention for their ease of fabrication, lightweight, semi-transparency, flexibility, and low-cost.[1–4] The progress in the development of novel organic materials, surface morphology, and suppressed saturation current have boosted the power conversion efficiency (PCE) of OSCs from 12% to over 17% in the last two years.[5–8] Recently, Zou and co-workers synthesized state-of-the-art nonfullerene material Y6 (more details can be found in ref. [4]).[8] Y6 shows a near-infrared region (NIR) absorption with a peak at around 880 nm and has the lowest unoccupied molecular orbital (LUMO) and a highest occupied molecular orbital (HOMO) level of −4.10 and −5.65 eV, respectively. By combining Y6 with the widely used polymer donor materials poly[(2,6-(4,8-bis(5-(2-ethylhexyl-3-fluoro)thiophen-2-yl)-benzo[1,2-*b*:4,5-*b*′] dithiophene))-alt-(5,5-(1′,3′-di-2-thienyl-5′,7′-bis(2-ethylhexyl)benzo[1′,2′-*c*:4′,5′-*c*′] dithiophene-4,8-dione)] (PM6) in a conventional device structure of ITO/PEDOT:PSS/PM6:Y6/PNDIT-F3N/Ag, efficiencies over 15% have been achieved.[8] Zou and co-workers further modified Y6 into another novel advanced nonfullerene acceptor material N3.[8,9] With consideration of its advanced photovoltaic (PV) properties, N3 is currently the most promising nonfullerene acceptor material for large-scale commercial fabrication of OSCs. A record PCE of 15.8% has been achieved by PM6:N3-based OSCs in a conventional device structure.[8] However, as the conventional device structure usually exhibits poor device stability, it is worth investigating the PM6:N3 combination in the more stable inverted device structure, which has not yet been explored.[10,11]

The OSC usually consists of three different layers including an active layer in the middle and the electron transport layer (ETL) and hole transport layer (HTL) on each side to help the charge transport (CT). The ETL and HTL are required to effectively transfer the electrons and holes generated from the active layer to each electrode.[12] In OSCs with an inverted device structure, the most commonly used ETL is zinc oxide (ZnO). ZnO is an II–VI material with widespread applications ranging from solar cells, light-emitting diodes, sensors to piezoelectric devices, and photocatalyst.[13] Its high electron conductivity and relatively low hole conductivity makes it an appealing ETL for thin-film solar cells.[14] It should, however, be noted that ZnO has shown to exhibit a high photosensitivity caused by the presence of surface defects.[15–17]

In OSCs, the ZnO ETL is fabricated using methods such as spin-coating, thermal evaporation, and chemical vapor deposition.[18–20] Although these techniques are faster and have a better growth rate, atomic layer deposition (ALD) has recently gained significant interest. This is due to its self-limiting nature, which results in precise control over the thickness, uniformity, and its

G. K. Poduval, L. Duan, Dr. M. A. Hossain, B. Sang, Y. Zhang, Prof. A. Uddin, Prof. B. Hoex
School of Photovoltaic and Renewable Energy Engineering
University of New South Wales
Sydney, NSW 2052, Australia
E-mail: a.uddin@unsw.edu.au; b.hoex@unsw.edu.au

Prof. Y. Zou
College of Chemistry and Chemical Engineering
Central South University
Changsha 410083, P. R. China
E-mail: yingpingzou@csu.edu.cn

The ORCID identification number(s) for the author(s) of this article can be found under https://doi.org/10.1002/solr.202000241.

DOI: 10.1002/solr.202000241

compatibility with vacuum systems. Moreover, the relatively low substrate temperatures (<200 °C) required for ALD permits the growth of ETL on temperature-sensitive substrates. ALD has been successfully used in a wide range of applications, including catalysis,[21] energy storage,[22] semiconductor,[23] and PV devices.[24] There have been some demonstrations of use of ALD for OSCs[25–27] which are dealt in greater detail in a review article by Hossain et al.[24] Nonetheless, there are only limited reports of its application for the growth of ZnO layer in OSCs."

Wang et al. demonstrated that 36 nm ALD ZnO deposited at 80 °C capped with Ag on a P3HT:PCBM OSC results in 4.18% efficiency.[28] Stakhira et al. showed a 2.5-fold improvement in efficiency by incorporating thin ALD ZnO capped with Al electrode on a nickel phthalocyanine (NiPc) without an anode layer.[29] When a similar approach was carried out by Frankenstein et al. for PCDTBT:PCBM-based OSCs, an efficiency enhancement from 2.75% to 3.5% was observed.[30] Kim et al., on the other hand, demonstrated that just 2 nm ALD ZnO enhanced the stability and performance of OSCs.[31]

The bandgap and electrical conductivity of the low work function ZnO can be easily tuned by doping.[32] By controlling the dopants, the electrical properties can be changed from an n-type semiconductor to a metal-like degenerate semiconductor without significant loss of optical transparency. The optical bandgap and short-wavelength transparency can also be increased due to the Burstein–Moss (BM) effect, resulting from higher carrier concentration of the degenerately doped ZnO.[33] These properties make doped ZnO films very interesting for solar cell applications.[34] Group III elements, such as Al,[35,36] Ga,[37] and In[38,39] when substituted for Zn can enhance the n-type properties of ZnO. Incorporation of these elements mainly creates shallow defect levels, which significantly improve the conductivity of ZnO. Al-doped ZnO has been the most commonly used material including in Si solar cells for its application as a transparent conductive oxide and as an ETL.[40–42] Other dopants, such as Mg,[43] Ni,[44] B,[45,46] Co,[47] Zr,[48,49] Ge,[50] Hf,[51] Sn[52] have also been investigated. Among these dopants, Zr^{4+} (0.84 Å) has the comparable ionic size to Zn^{2+} (0.74 Å) and the ability to donate two electrons with minimum lattice distortion into the ZnO host lattice.[48,49,53–55] Smaller ionic radii dopants, such as Al and B tend to occupy interstitial Zn defects ($Zn_i^{\cdot\cdot}$), whereas Zr undergoes substitutional doping due to its comparable size without reduction of Zn native donors.[32] Zr also does not form secondary intermetallic phases upon binding to Zn atoms.[56] Therefore, Zr is a promising dopant for ZnO.

A few material studies have been reported about Zr doping in ZnO using ALD, mainly focusing on the application in light-emitting diodes and transistors.[48,49,53] It suggests that Zr doping enhances the electrical and optical properties of ZnO, a trend similar to that observed in indium oxide. For solar cell applications, only the influence of Zr doping in In_2O_3[54,55] has been reported, but Zr-doped ZnO is yet to be studied.

In this work, we report the first successful demonstration of OSCs with Zr-doped ZnO layer as ETL. We achieved an efficiency enhancement of ≈1% compared with undoped ZnO as ETL in inverted PM6:N3-based OSCs. A complete investigation was carried out using a DFT study, material synthesis and analysis, and device integration. This article starts with the first-principles density functional theory (DFT) calculations to understand the electronic band structure properties of Zr-doped ZnO. Subsequently, we present the optimization of the Zr doping into ZnO using ALD technology and found Zr doping in ZnO at an optimized 2.4% Zr in ZnO can improve electrical properties compared with an undoped Zn. OSCs were fabricated with an inverted structure of ITO/(ETL)/PM6:N3/MoO_3/Ag using both undoped ZnO and Zr-doped ZnO as ETL. It was found that the OSCs with the doped ZnO layer had a lower series resistance (R_s), lower recombination between the ETL and active layer, and enhanced current extraction compared with the reference devices with an undoped ZnO ETL resulting in an ≈1% absolute increase in efficiency from ≈13% to ≈14%.

2. Experimental Section

The computation and experimental work are divided into three parts, as shown in **Figure 1**. First, the DFT simulations were carried out to model doped ZnO. Second, doped ZnO layers were grown by ALD for material characterization. Finally, the OSCs device was fabricated and characterized.

2.1. DFT Calculations

The first-principles DFT calculations were performed using the Vienna Ab-initio Simulation Package (VASP).[57] The interactions between valence electrons and ionic cores were described by the Perdew–Burke–Ernzerhof (PBE)[58] forms of the generalized gradient approximation (GGA) functionals, as implemented in VASP. The elemental electron configurations in the pseudopotentials were set to be Zn ($3d^{10}4s^2$), O ($2s^22p^4$), and Zr ($4s^24p^65s^24d^2$). A plane-wave basis set with a kinetic energy cutoff of 500 eV was used for all calculations. Integration over the Brillouin zone for the $3 \times 3 \times 2$ ZnO supercell (72 atoms) was conducted using a $4 \times 4 \times 3$ k-point mesh generated by Monkhorst–Pack scheme and using Gaussian smearing of 0.01 eV,[59] which yielded converged total energy within 1 meV, consistent with previous work on transition metal oxides. A rotationally invariant on-site Coulomb correction (GGA + U) was applied to the Zn 3d electrons using the Dudarev's formalism,[60] with an effective U value of 10.5 eV, in line with published literature and which gives overall agreement of the band structure and density of states (DOS) with experiments. ZnO was substitutionally doped with Zr at Zn site with a 2.7 atomic percent (at%) to investigate the electronic band structure characteristics. All calculations were carried out using spin-polarization as ZnO can be ferromagnetic in both its pristine form[61] as well as after doping.[62] The 72 atoms ZnO supercell was chosen for the Zr dopant study because it provides a small Madelung potential of 0.036 eV, implying a small charge–charge self-interaction error for the Zr-doped ZnO.[63–68]

2.2. ALD Zr:ZnO

Boron-doped Czochralski (Cz) single-side polished Si (100) wafers were cleaned using the standard Radio Corporation of America (RCA) 1 cleaning (NH_4OH: H_2O_2:H_2O at 1:1:5 ratio for 6 min at 85 °C) to remove organic impurities and RCA-2 cleaning (HCl: H_2O_2:H_2O at 1:1:5 ratio for 6 min at 85 °C) to remove any

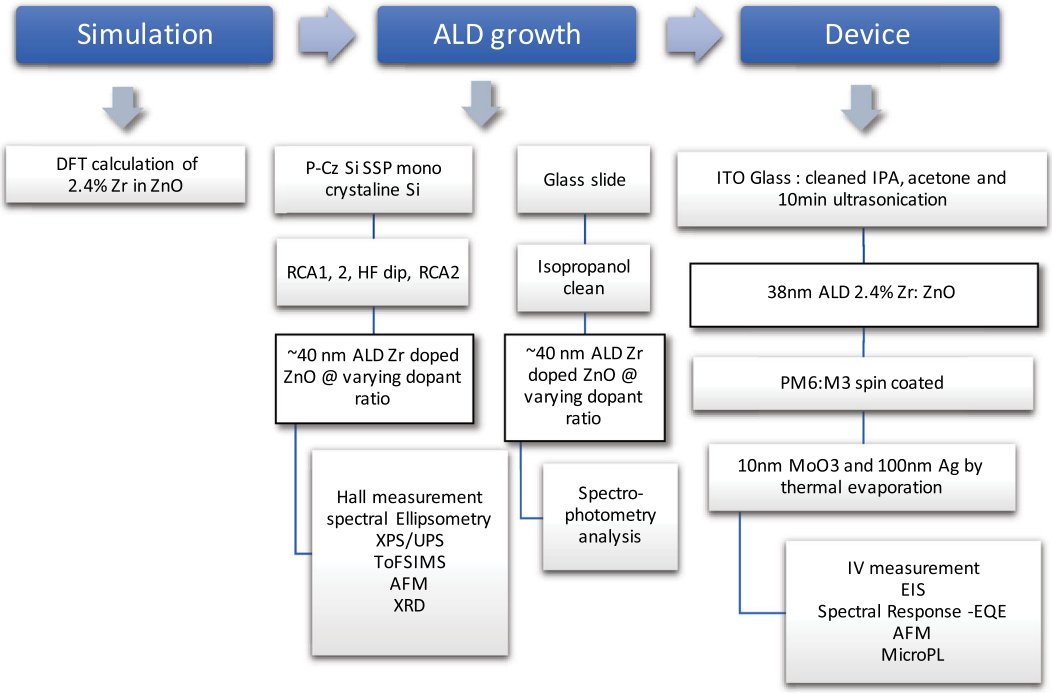

Figure 1. Schematic representation of the process flow used in this work.

metallic impurities.[69] Subsequently, the wafers were dipped into 2% hydrofluoric acid (HF) to remove the native oxide from the surface, and a fresh oxide was regrown by dipping in RCA-2. This chemical oxide was essential for the nucleation of metal oxide growth during ALD. Metal oxides were also simultaneously deposited onto a clean glass substrate (cleaned using isopropanol) for optical characterization, as shown in Figure 1.

Around 40 nm of ZnO with various doping concentrations of zirconium (Zr) was carried out using a Veeco Fiji G2 ALD reactor, which was equipped with an in situ spectroscopic ellipsometer (J. A.Woollam M-2000). Thermal ALD was used to deposit ZnO using diethyl zinc [DEZ, $Zn(C_2H_5)_2$, Sigma Aldrich] as Zn precursor (precursor at room temperature, pulse time: 0.06 s, purge time:10 s), and water (precursor at room temperature, pulse time:0.06 s, purge time:10 s) as the oxygen precursor at a deposition chamber temperature of 150 °C at a growth rate of 1.6 Å per cycle. ZrO_2 was also thermally grown at the same substrate temperature using tetrakis(dimethylamido)zirconium(IV) [TDMAZr, $(CH_3)_2N_4Zr$, Merck] precursor (precursor temperature 75 °C, pulse time: 0.1 s, purge time:15 s) and water (pulse time: 0.06 s, purge time: 15 s) as the oxygen precursor[48,70–72] at a growth rate of 1.39 Å per cycle. The respective growth rates were obtained from fitting the in situ spectroscopic ellipsometry measurements using a PSemi-M0 and two Gaussian oscillations to describe the dielectric function of the ZnO and ZrO_2 films. Zr doping in ZnO was achieved using a supercycle approach, as shown in **Figure 2**. This involves the *M* number of ZnO ALD cycles followed by *N* number of ZrO_2 cycles, where the *M*/*N* ratio was chosen depending on the desired Zr concentration. The various supercycle ratios used and the corresponding doping concentrations are shown in **Table 1**.

The Zr-doped ZnO was characterized ex situ using a Perkin Elmer Lambda 1050 UV/VIS-NIR spectrometer and a J.A. Woollam spectroscopic ellipsometer to determine the optical properties of the film. The resistivity and charge carrier density and mobility in the film was determined from Hall measurement using an HMS-5000 Hall effect measurement system (Ecopia) at room temperature, and a magnetic field of 0.5 T. Time-of-flight secondary ion mass spectrometry (ToF–SIMS) (TOF.SIMS 5, IONTOF) analysis in positive polarity by Bi^{3+} at 30 keV, sputter by Cs^+ beam of 500 eV was used to determine the distribution of Zr and Zn in the film. X-ray photoelectron spectroscopy (XPS) and ultraviolet photoelectron spectroscopy (UPS) (ESCALAB 250Xi Thermo Scientific, UK) at a power of 120 W (13.8 kV × 8.7 mA) at take-off angle of 90° using He I (21.2 eV) and He II (40.8 eV) UV source was performed to determine the elemental state and composition of the film grown. Atomic force microscopy (AFM) (Dimension ICON, Bruker) was performed over a scan area of 1 μm × 1 μm in tapping mode using a cantilever at a scan rate of 0.5 Hz using a SCANASYST-Air probe to determine the surface morphology of the samples. X-ray diffraction (XRD) (Empyrean I, Malvern Panalytical) using Cu K_α radiation of wavelength $\lambda = 0.1541$ nm was performed to obtain the crystallographic orientation of the thin films.

2.3. Device Fabrication

OSCs were fabricated using an inverted device structure consisting of ITO/ETL/active layer/ HTL/Ag. The MoO_3 layer was used as the HTL. The bulk heterojunction (BHJ) PM6:N3 layer was used as the active layer, where the PM6 and N3 were the donor and acceptor material, respectively. The ITO glass substrate was

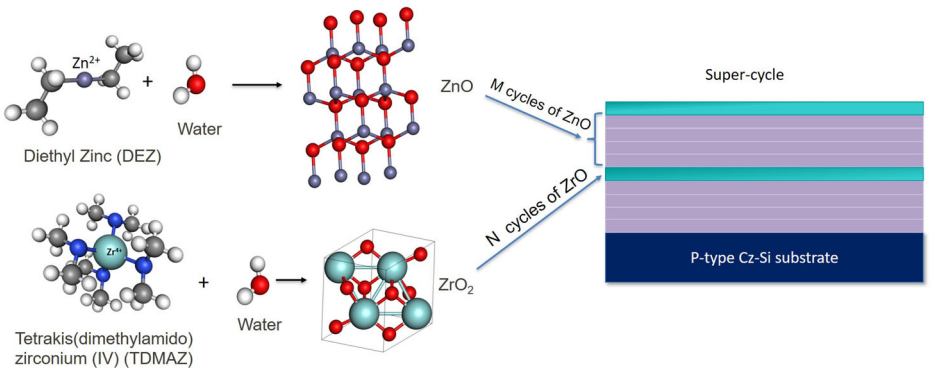

Figure 2. Pictorial representation of the supercycle process of the ALD grown of Zr-doped ZnO on a p-type Cz Si substrate. The substrate thickness to film thickness is not to scale.

Table 1. Zr atomic doping concentration for various ALD supercycle ratios. The Zr concentration was determined from XPS measurements.

ZnO:Zr ALD Cycles [M:N]	Zr [a%]
60:1	1.64
40:1	2.44
10:1	9.09
10:2	16.7
10:4	28.6

sequentially cleaned in an ultrasonication bath using 1) soapy deionized (DI) water, 2) pure DI water, 3) acetone, and 4) isopropanol. ALD undoped ZnO or Zr:ZnO was used as the ETL. The PM6:N3 active layer solutions were made from 10 mg PM6 and 12 mg N3 with a 1:1.2 wt ratio in a 17.6 mg mL^{-1} chlorobenzene solution with 0.5% vol CN as an additive. The active layer solution was stirred overnight inside an N_2-filled glovebox at 80 °C and then spin-coated at a rate of 2000 rpm for 1 min. After that, the coated samples were put into a vacuum chamber at a pressure of 10^{-5} Pa. The 10 nm thick film of MoO_3 and 100 nm thick film of silver were deposited to the sample surface through a shadow mask by thermal evaporation. The resulting device area was 0.045 cm^2.

2.4. Device Characterization

The current density–voltage (J–V) measurements were conducted using a solar cell I–V testing system from PV Measurements, Inc. (using a Keithley 2400 SourceMeter) under an illumination power of 100 mW cm^{-2} by an AM 1.5 G solar simulator. The device temperature was measured by GM1350 50:1 LCD infrared thermometer digital gun and maintained at around 25 °C. The electrochemical impedance spectroscopy (EIS) study was conducted by using an Autolab PGSTAT-30 to reveal interfacial properties. This characterization was conducted inside a glovebox using a frequency range of 106–100 kHz using a frequency analyzer module. A QEX10 spectral response system from PV measurements was used to measure the external quantum efficiency (EQE) of the solar cell devices. A Bruker Dimension ICON SPM with a scan size of "5 μm × 5 μm" and a scan rate of 0.512 Hz was used for AFM measurements to characterize the film surface morphology. Micro-photoluminescence (μPL) characterization was conducted on a home-built μPL system. The sample was excited by a pulsed optical parametric oscillator laser at 532 nm. For steady-state spectral PL, the signal was detected by Glacier X TE Cooled charge-coupled device spectrometer with a detection range of 200 to 1050 nm. For the time-resolved PL (TRPL) measurements, the signal was detected by id110 VIS 100 MHz photon detector.

3. Results and Discussion

First principle DFT simulations were carried out to understand the impact of Zr doping into ZnO, especially on the electronic DOS. The DFT results shown in **Figure 3** compare the partial DOS of undoped and Zr-doped ZnO. It can be observed that the conduction band of a pure ZnO is mainly comprised of O 2p orbitals and Zn 4s states, whereas the valence band was mainly contributed by O 2p and Zn 3d states. Upon Zr doping, an additional contribution of Zr 3d orbital predominates the conduction band, causing the Fermi level to move to the conduction band, confirming the defect states originate from the Zr 3d states (Figure 3b). The spike in DOS of the conduction band in Zr-doped ZnO manifests to change in ZnO to a degenerate semiconductor, thus increasing the carrier concentration and increasing the electron mobility of ZnO.

Figure 4 shows the in situ spectroscopic ellipsometry results obtained during the ALD supercycle process. It can be observed that after the initial temperature stabilization of ≈7 min, the ALD growth proceeded almost linearly as a function of time with superimposed oscillations due to the self-limiting half-reactions of the ALD process. When the DEZ or TDMAZr molecule binds to the surface, the thickness is observed to increase. Upon reacting with H_2O, the thickness reduces as the formed metal oxide layer has a smaller molecular size than the precursor. The difference in thickness between the initial and final value of each cycle represents the thickness grown in each cycle. The growth per cycle was calculated by taking an average change in thickness for 20 cycles.

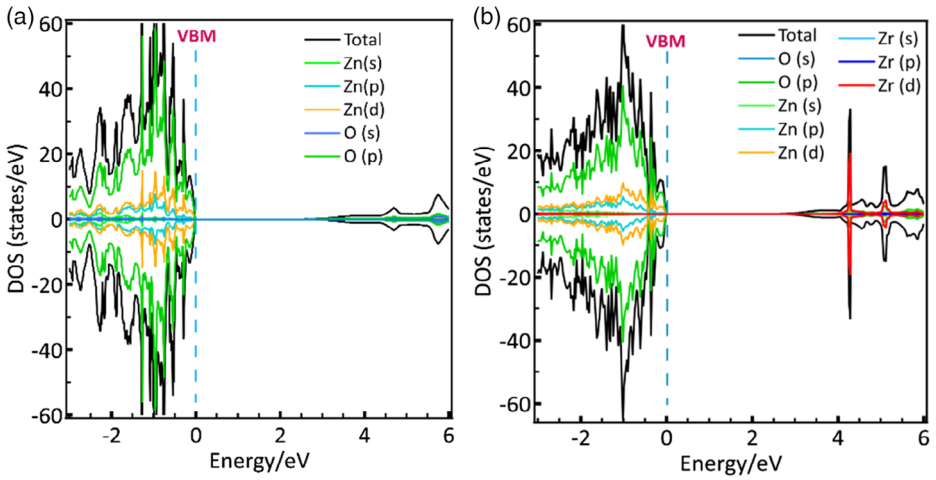

Figure 3. Calculated total and projected electronic DOS for Zr, Zn, and O of a) intrinsic ZnO and b) Zr-doped ZnO. The dashed vertical line represents VBM of ZnO and Zr-doped ZnO.

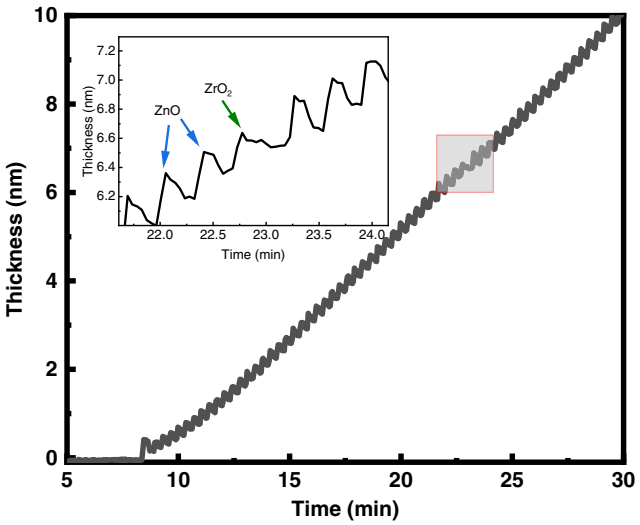

Figure 4. Thickness as a function of time measured during the ALD growth of Zr-doped ZnO. The film thickness was measured in situ using spectroscopic ellipsometry. The inset shows a magnification of the area of the graph indicated by the gray square showing six ZnO and one ZrO_2 ALD cycle.

UV–vis spectrophotometry measurements were carried out to study the optical properties of undoped and Zr-doped ZnO films. The Tauc plot[73] of ZnO (**Figure 5**a) shows that the bandgap increases with increased doping for low doping concentrations. The lowest bandgap of 3.2 eV was observed for undoped ZnO and a maximum of 3.43 eV for 9% Zr in ZnO. The blue shift of optical bandgap upon doping is due to the BM effect due to degenerate band filling of the conduction band along with the increased carrier concentration, as also observed in the DFT simulations (Figure 3).[74]

The carrier mobility as a function of the Zr doping concentration shown in Figure 5b indicates that the carrier mobility reached a maximum of 19 $cm^2 Vs^{-1}$ for a Zr doping of 2.4%; this is similar to that observed by Herodotou et al.[71] The carrier mobility significantly decreases for higher doping concentrations. This abrupt reduction in mobility is attributed to the reduction in carrier concentration due to the segregation of Zr ZrO_2 instead of replacing Zn^{2+} sites is inhibiting the effective doping of ZnO. With an increase in ZrO_2:ZnO ALD cycle ratio, the extent of segregation increases, thus reducing the ability of Zr to donate the two free electrons. At 4% Zr a theoretical approximately tenfold enhancement should be observed if all Zr atoms donate two electrons. This is not observed in this case and could relate to the enhanced segregation of Zr as ZrO_2. Annealing at high temperatures or modifying the growth by the simultaneous flow of Zn and Zr precursor at controlled flowrates in ALD could be an approach to overcome this issue.

The elemental profiles of ToF–SIMS (**Figure 6**a) show a uniform distribution of Zn^+ and O^+, whereas ZrO^+ and Zr^+ oscillate between high concentration and low concentration. These fluctuations correspond to the layers of ZrO_x in the film formed during the ALD supercycle. The intentionally grown SiO_2 is observed at the interface and plays a vital role in ensuring the nucleation of the ZnO ALD process on the Si substrate.

The XPS spectra of Zn 2p peak (**Figure 7**a) corresponding to ZnO (2p3/2 centered at 102.8 eV) shows no changes upon doping with Zr.[75] Although the peak intensities have changed, their full width at half maximum (FWHM) and the ratio of the 3d doublet peaks remains constant for all the doping concentrations. Moreover, a consistent Δ 3d = 22.97 eV confirms that Zn remains in the ZnO form, i.e., in +2 oxidation state. The Zr 3d line position of 3d5/2 shifted from an elemental state of 178.9 eV to 182.1 eV while still maintaining the same Δ 2p of 2.43 eV. This confirms that all Zr is present in the ZrO_2 state (Figure 7b), i.e., in the +4 oxidation state. The ratio between the two doublet peaks, FWHM, and separation, did not have much change, indicating that Zr in all the samples was in the same state. Figure 6b shows the density and occupancy of electronic states in the valence band. The leading edge of the valence-band spectra Ev of the Zr-doped ZnO moves away from 0 with increasing Zr concentration. The presence of Zn4+ ions in the ZnO lattice creates additional energy levels near the valence band of ZnO.

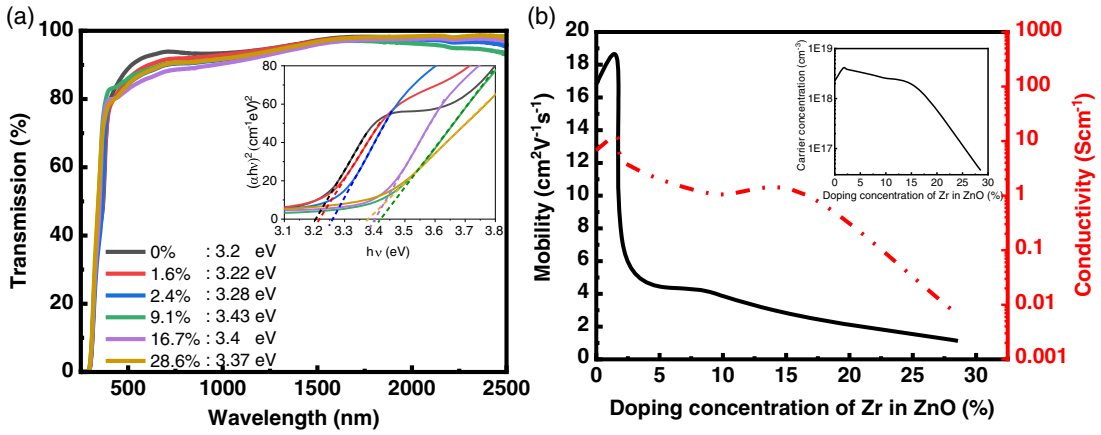

Figure 5. a) Transmission spectra of the doped ZnO normalized with an uncoated glass. Inset: Tauc plot of the Zr-doped ZnO showing the bandgap change upon doping. b) Mobility, conductivity, and carrier concentration as a function of the Zr-doping concentration. The inset shows the carrier concentration as a function of the Zr-doping concentration.

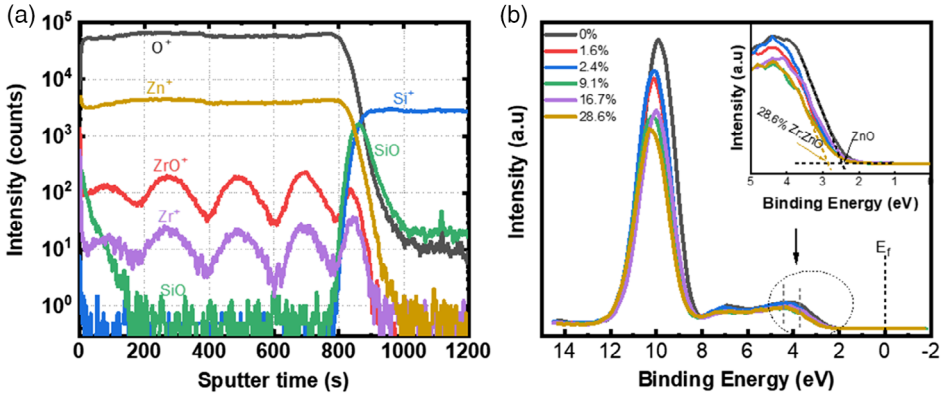

Figure 6. a) ToF-SIMS depth profile of a Zr-doped ZnO film with a Zr concentration of 2.4%. b) XPS valence spectra of all the Zr-doped ZnO samples showcasing the shift in VBM upon an increase in doping concentration.

This change also contributes to the increase in bandgap along with increased states in the conduction band.

The XPS spectra of O 1s (Figure 7c) were fit using three Gaussian peaks 529 eV, 531 eV, and 532.4 eV binding energy (BE). The peak at 529.8 eV corresponds to O^{2-}ions in the sample surrounded by Zn or Zr ions. The peak at a 532.4 eV BE was mainly attributed to the absorption of H_2O or loosely bound O ions on the surface. The final BE of 531 eV mainly represents oxygen vacancies (V_o). It can be observed that the O^{2-} peak has a shift of +0.3 eV and the V_o peak has a shift ≈0.5 eV. The intensity of V_o peak was observed to increase with increased doping, indicating that a significant amount of oxygen vacancies were formed during the fabrication of Zr-doped ZnO. The addition of 1.6% Zr significantly enhances the bulk oxygen vacancy density. The O^{2-} concentration, in contrast, is highest for a 1.6% Zr concentration and decreases with a further addition of Zr. The XPS spectra of C1s (Figure 7d) shows that the intensity of C—O—C bond (centered at 286.5 eV) was significantly lower for undoped ZnO, indicating that the amount of dangling bonds formed is minimum. Upon Zr doping, the ratio between C—O—C and C—C is negligible, indicating that there is no significant change in the dangling bond density upon Zr doping.

The UPS spectra (**Figure 8**) of the undoped and doped ZnO was used to determine the work function using the following equation

$$\Phi = h\nu - E_{\text{cutoff}} + E_{\text{fermi}} \quad (1)$$

where Φ is the work function, h is the plank constant, ν is the frequency of the excitation UV light, E_{cutoff} is the secondary electron cut-off energy, E_{fermi} is the Fermi level. The Fermi level for ZnO films with a Zr concentration of 0%, 1.6%, 2.4%, 9.1%, 16.7%, and 28.6% was 5.17, 5.16, 5.17, 5.22, 5.24, 5.25 eV, respectively. It can be observed that there was no significant change in the work function for Zr concentrations up to 2.4%. Although the Fermi level was observed to move away from the valence band maximum (VBM) as shown in Figure 8–right. This indicates that the conduction band is closer to the Fermi level for Zr-doped ZnO compared with undoped ZnO in good agreement with the predictions from DFT.

Figure 9 shows a 2D AFM image of the ALD-grown ZnO in undoped and Zr-doped form. The films are shown to be dense and have a smooth surface. The grain size for pure ZnO is seen to be round, uniform, and highly dense. With an increase in

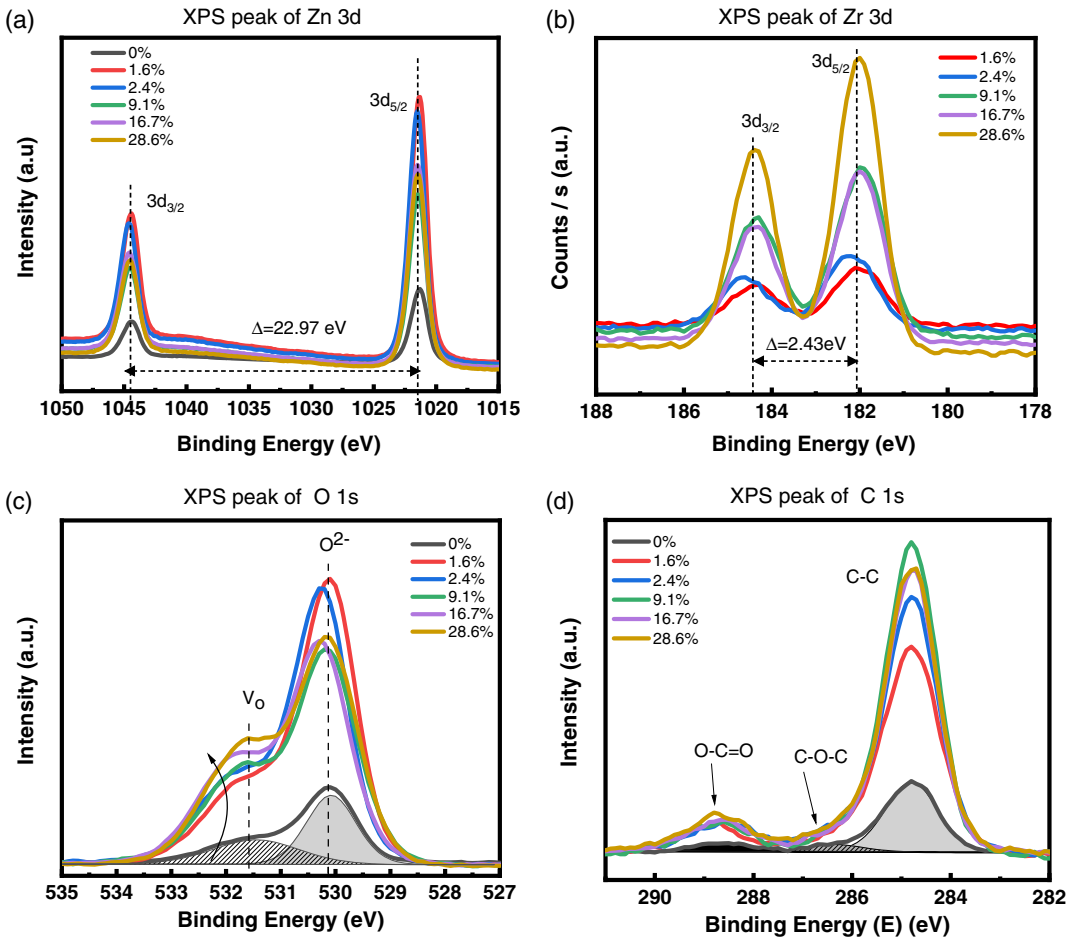

Figure 7. XPS spectra of a) Zn 2p and b) Zr 3d; c) O1s and d) C 1s peaks in the doped sample.

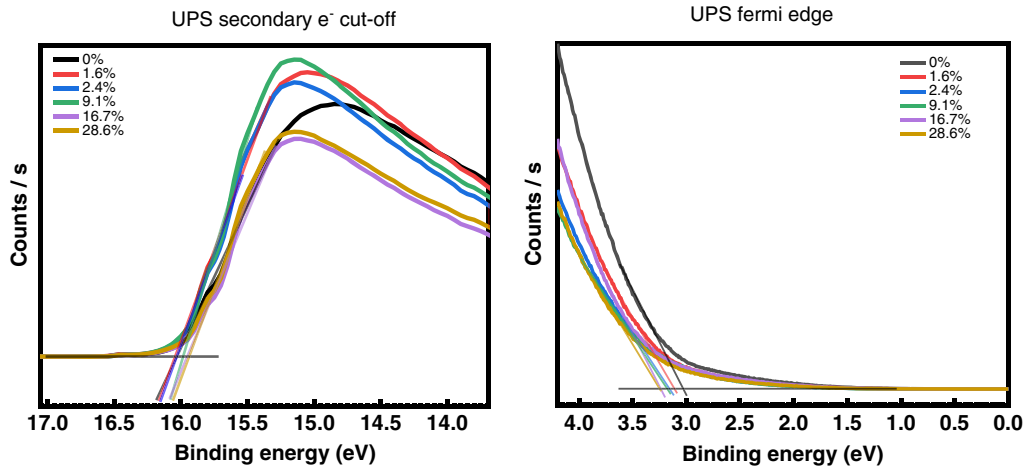

Figure 8. UPS spectra of the Zr-doped ZnO films with varying doping concentration. Left: Secondary electron cut-off energy of UPS used to determine the work function. Right: Fermi edge of UPS used to determine the valence band edge.

Zr doping, the grains are seen to be more and more elongated. At Zr concentration of 9.1%, the features are observed to be more disc-like shaped with an anisotropic growth direction along (110) as also observed from the XRD measurements shown in **Figure 10**. Beyond this, the film becomes denser and more amorphous.

Figure 10 shows the XRD patterns of Zr-doped ZnO with various doping concentration as well as undoped ZnO. The

characteristic diffraction peak of the wurtzite phase of ZnO (ref. JCPDS:36–1451) is similar to that of the ALD-grown undoped ZnO. However, the peaks are broader and have a lower intensity as the film is mainly polycrystalline with majority grains oriented along (100), (002), (101) direction. It can be observed that with a 1.6% Zr-doping, the grains reorient to increase its directionality along (100), (002). Also, with an increase in Zr concentration, the grains tend to align more toward (110). At 9.1% Zr, the polycrystals prefer to orient themselves along (110) and its contribution from (002) significantly reduces. Moreover, a shift from $2\theta = 56.6°$ to 55.6° was observed due to the change in lattice parameters in the ZnO crystalline structure due to Zr doping. With further increase in Zr concentration, the film becomes more amorphous and loses its crystalline orientation.

It has been observed that the sample with improved electrical properties without compromising on optical transparency was 2.4% Zr in ZnO in comparison to undoped ZnO. This film has similar morphology and crystallography as that of undoped ZnO with increased oxygen vacancies. Hence, this ALD-grown film was selected as the ETL for the OSC.

The device structure and the chemical structure of the PM6 and N3 is shown in **Figure 11**a,b. The normalized absorption spectrum and the energy-level diagram of the PM6 and N3 are shown in Figure 11c,d. The ALD Zr-doped ZnO with the optimized ratio, or undoped ZnO was used as the ETL in the device. The device based on ALD Zr:ZnO ETL and the control device based on ALD pure ZnO ETL were compared from a device performance perspective.

The *J*–*V* curves for both types of devices are shown in **Figure 12**a and the corresponding PV parameters including open-circuit voltage (V_{oc}), short-circuit current density (J_{SC}), fill factor (FF), PCE, shunt resistance (R_{sh}), and series resistance (R_s) are listed in **Table 2**. It can be seen that the Zr-doped ZnO-based devices show a significantly better device performance than undoped ZnO-based devices. The champion PCE of ALD Zr-doped ZnO-based devices was 14.7% with an average V_{oc} of 0.83 V, J_{sc} of 26.50 mA cm^{-2}, and FF of 0.653. In comparison, the device performance of undoped ZnO-based control devices was lower with an average PCE of 13.3%, a V_{oc} of 0.84 V, J_{sc} of 26.01 mA cm^{-2}, and FF of 0.606. This performance enhancement can mainly be attributed to an increased FF value using the

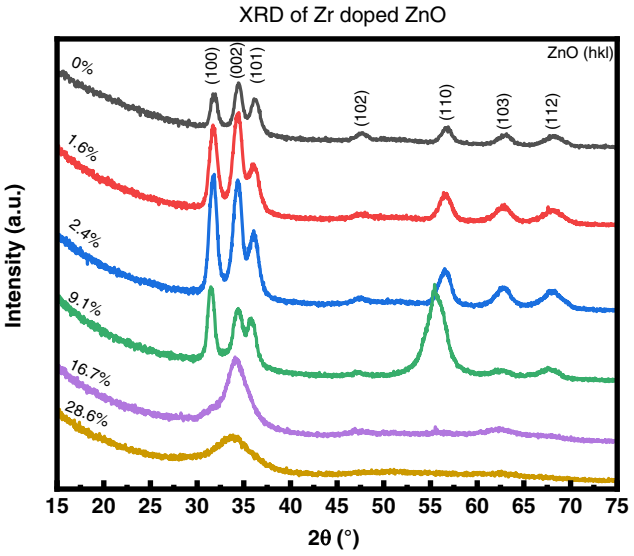

Figure 10. XRD spectra of the Zr-doped ZnO films with varying doping concentration.

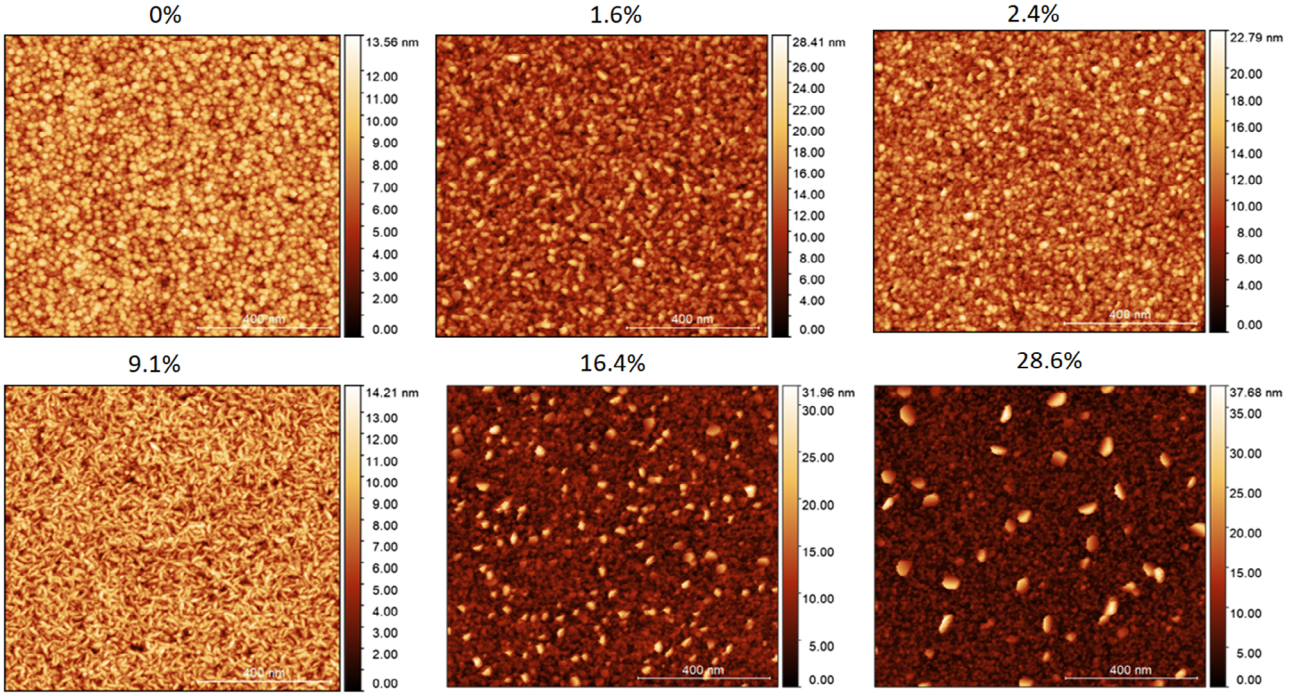

Figure 9. AFM image of ALD-grown Zr-doped ZnO films with various doping concentration.

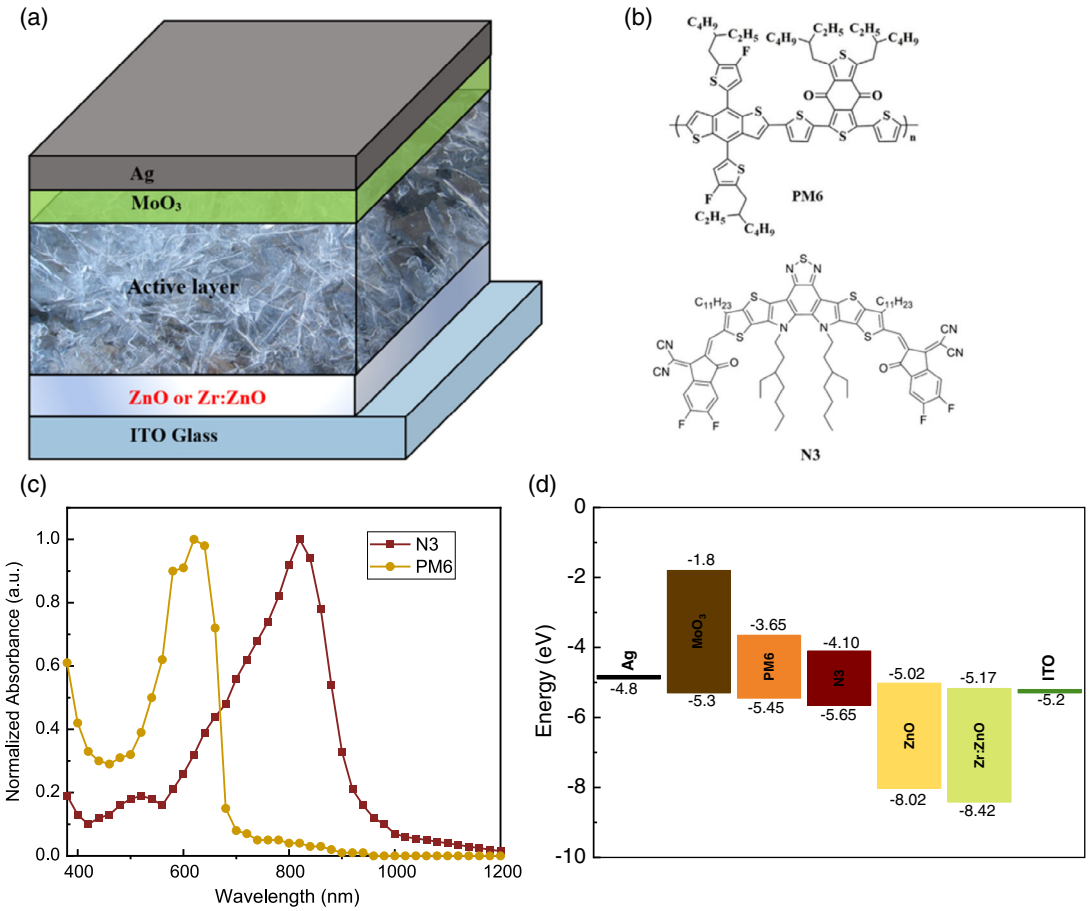

Figure 11. a) Schematic diagram of the inverted OSC device structure. b) Chemical structure of the PM6 and N3 compounds used in the active layer. c) Normalized absorption spectrum and d) energy band diagram of the device. The energy level of ZnO and Zr-doped ZnO is calculated using UPS (refer Figure 10).

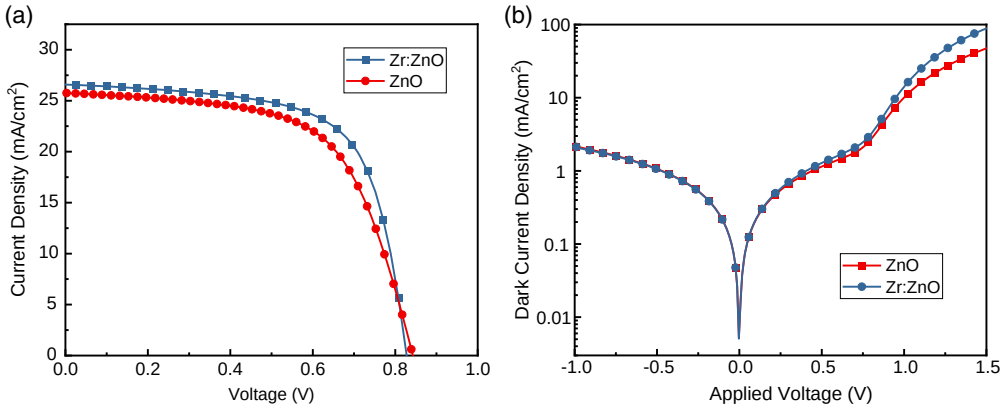

Figure 12. a) Current–voltage (J–V) curves of both ZnO and Zr:ZnO-based devices tested at room temperature under one-sun test condition (AM1.5 G illumination at 100 mW cm^{-2}). b) Dark current–voltage for both ZnO and Zr:ZnO-based devices.

ALD Zr-doped ZnO layer as the ETL, where the changes in V_{oc} and J_{sc} were minimal. For device with Zr-doped ZnO as the ETL, the R_s was found to be significantly lower by around 37% from 6.5 to 4.1 Ω cm^2, whereas the R_{sh} decreased by around 11% from 518.3 to 461.1 4.1 Ω cm^2. The change in the R_{sh} and R_s both affect the FF of a device. A decrease in R_s can result in an increase in FF, whereas a decrease in R_{sh} can cause a decrease in FF. Using a one diode solar-cell model with an ideality factor of 1, the changes in FF resulted from the changes in R_s and R_{sh} can be estimated. In this case, the decrease in R_s resulted in a

Table 2. V_{oc}, J_{sc}, FF, PCE, R_{sh}, and R_s of devices based on both ZnO and Zr:ZnO ETL. The parameters were measured at room temperature under one-sun test condition (AM1.5 G illumination,100 mW cm^{-2}) and the average value and the standard deviation were determined from the measurement of at least five devices.

Device	V_{oc} [V]	J_{sc} [mA cm^{-2}]	FF	Average (Best) PCE	R_{sh} [Ω cm^2]	R_s [Ω cm^2]
ZnO	0.84 ± 0.00	26.0 ± 0.9	0.61 ± 0.01	13.3 ± 0.4%(13.8%)	518.3 ± 42.3	6.5 ± 0.6
Zr:ZnO	0.83 ± 0.00	26.5 ± 0.5	0.65 ± 0.01	14.3 ± 0.4%(14.7%)	461.1 ± 20.8	4.1 ± 0.4

10% relative increase in FF, whereas the decrease in R_{sh} only resulted in a 1% relative decrease in FF. Herein, the observed increase in FF may mainly be attributed to a decrease in the R_s.[7,76,77] To investigate the performance enhancement, dark J–V measurements were conducted for both devices. Figure 12b shows the dark J–V measurements for both devices. In the diagram, when the device under reverse voltage bias at −1.0 V, the current density value can represent the leakage current value in the device.[78] In contrast, the slope of the dark J–V curve at a high-voltage range (>0.75 V) reveals the R_s of the device, where a steeper curve represents a lower R_s.[79] From Figure 3a, it was found that the leakage current value in both types of devices was very similar, whereas the ALD Zr-doped ZnO-based device shows a lower R_s than control device. The result is consistent with the observation from the light J–V measurements.

EQE measurements were then conducted for both types of devices (**Figure 13**a). It was observed that the ALD Zr:ZnO-based device showed a slightly higher EQE in the 400–800 nm range than the control devices, which indicates that the electrical current generation in the ALD Zr:ZnO-based device can be slightly more efficient than the control device. The integrated J_{sc} value from EQE was around 25.42 mA cm^{-2} for the control device and 25.96 mA cm^{-2} for the device with the Zr-doped ZnO as the ETL. The result is consistent with the light I–V, indicating lower optical loss as suggested by higher bandgap value for the Zr-doped ZnO films compared to undoped ZnO (Figure 12a).

By combing the light and dark J–V measurements, the charge carrier extraction possibility (P) analysis was conducted for both types of devices. In this analysis, the photocurrent density (J_{ph}) and the effective voltage (V_{eff}) can be calculated using the following equations[80–82]

$$J_{ph} = J_L - J_D \tag{2}$$

$$V_{eff} = V_{oc} - V_{bias} \tag{3}$$

where J_L represents the light current density under one-sun test condition, J_D represents the dark current density under dark test condition, and V_{bias} represents the applied external voltage bias. The analysis assumes that all excitons generated in the active layer can be effectively separated and collected at a high effective voltage (>1.0 V). Therefore, the J_{ph} value reaches a maximum value which is also called as saturation current density (J_{sat}) when V_{eff} is higher larger than 1.0 V. The charge carrier extraction possibility value then can be extracted using the following equation which represents the ratio between the real maximum current density and the theoretical maximum current density in the device[80]

$$P(I, V_{eff}) = \frac{J_{ph}(I, V_{eff})}{J_{ph.sat}(I)} \tag{4}$$

The charge carrier extraction possibility analysis can reveal the mechanism behind the current loss in the current extraction process, which is closely related to the carrier transport layer and its interface with the active layer.[83] The J_{ph} to V_{eff} curve for both types of devices is shown in Figure 13b, and the corresponding J_{sat} and P values are listed in **Table 3**. It is apparent to find that the Zr:ZnO-based device shows a higher J_{sat} and P value than the control device, which indicates that the ALD Zr:ZnO-based ETL can contribute to a more efficient current extraction process than ZnO-based ETL. It is reasonable that Zr:ZnO-based device showed higher J_{sat}, as the Zr:ZnO layer had a slightly higher bandgap than undoped ZnO layer, which indicates a lower light absorption in Zr:ZnO layer. When

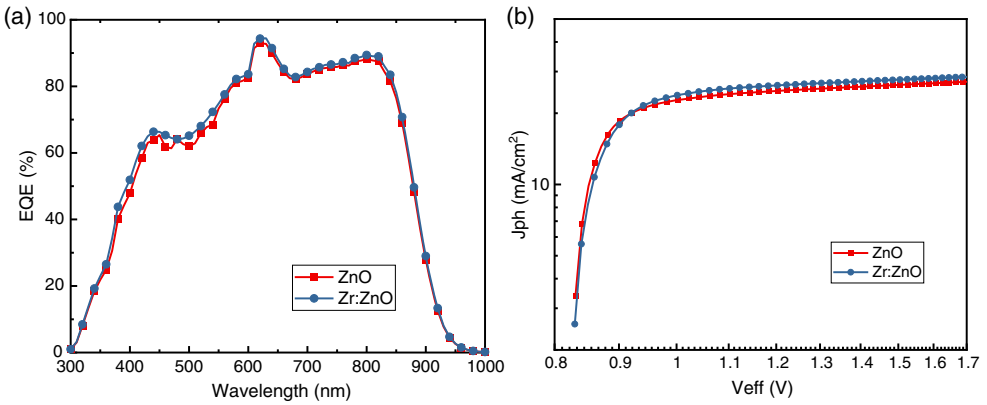

Figure 13. a) EQE as a function of wavelength and b) photocurrent (J_{ph}) to effective voltage (V_{eff}) for both ZnO and Zr:ZnO devices.

Table 3. Charge extraction probabilities (P), and saturation current density (J_{sat}) of both ZnO and Zr:ZnO-based devices.

Device	J_{sat} [mA cm^{-2}]	P
ZnO	27.6	88.1%
Zr:ZnO	28.9	90.8%

replacing ZnO with Zr:ZnO layer, the absorption loss in ETL is lower, thus more light passes through the ETL and can be absorbed in the absorber layer. The result further confirms the higher EQE measured for the ALD Zr:ZnO-based device.

On the other hand, steady-state photoluminescence (PL) and TRPL measurements were conducted for both types of devices to investigate the performance enhancement further. **Figure 14**a,b show the steady-state PL spectrum and normalized TRPL spectrum for both types of devices under a 532 nm laser excitation, respectively. In the steady-state PL spectrum, the PL intensity can represent the number of excitons in the device. A higher PL intensity usually implies a more significant number of undissociated excitons.[84,85] From Figure 14a, the difference between the PL spectrum of each type of device is negligible, which reveals that the replacement of ZnO with Zr:ZnO as ETL has no significant effect on the exciton dissociation process in the device. To analyze TRPL results, a biexponential decay model was used to fit the spectrum to find the excited state lifetime in the device[86,87]

$$Y = A_1 \exp\left(-\frac{t}{\tau_1}\right) + A_2 \exp\left(-\frac{t}{\tau_2}\right) + y_0 \quad (5)$$

where t is the time, A_1 and A_2 are the amplitudes, y_0 is the y-axis intercept, τ_1 and τ_2 represent the fast and slow lifetimes. The excited lifetime can reveal the energy transfer process inside the active layer.[84,88] As the Förster resonance energy transfer (FRET) offers an alternative nonradiative pathway between the donor and acceptor, a lower lifetime usually indicates a more efficient energy transfer process.[89,90] The estimated fast and slow lifetime for both devices were very similar at 0.12, and 1.15 ns for the control device and 0.11 and 1.12 ns for the ALD Zr:ZnO-based device. It was found that the difference in the lifetime values between these two types of devices was also negligible, which implies that the replacement of ZnO with Zr:ZnO as ETL also has a neglectable effect on the carrier lifetime in the device. Moreover, EQE spectrum tails, also called "Urbach tail", were used to estimate the Urbach energy for both types of devices, as shown in **Figure 15**a. The Urbach energy in the active layer of both types of device can be estimated by fitting the EQE tail with an exponential growth model[91–93]

$$EQE(E) \propto \alpha(E) \propto \exp\left(\frac{E}{E_U}\right) \quad (6)$$

where α, E, and E_U are the light-absorbing coefficient, the photon energy, and the estimated Urbach energy, respectively. As the photocurrent response edge of the device is dependent on the accepter material N3 with an optical bandgap of 1.33 eV, any further response lower than 1.33 eV observed in EQE spectrum was attributed to the excitation of the CT states which can indicate the energetic disorder in the active layer.[8,94,95] As a result, the Urbach energy obtained for these two types of devices was almost identical at 26.2 meV. A similar Urbach energy implies that the replacement of ZnO with Zr:ZnO as ETL has a negligible effect on the energetic disorder in the device. AFM images are shown in Figure S1, Supporting Information. It is easy to find that the active layer on both types of ZnO shows a smooth surface, and the morphology of the active layer in both types of devices is very similar to each other. Thus, the replacement of ZnO with Zr:ZnO has a negligible effect on the formation of active layers on top, which can be the root reason for that it has less effect on the exciton dissociation process, energy transfer process, and energetic disorder in the device.

EIS measurements mainly focus on testing the response of the device under an external alternating current (AC).[96,97] The applied voltage selected for both types of devices was selected as 0.7 V, which is slightly lower than their V_{oc}. At a low voltage bias, traps in the active layer can respond to the modulated signal, whereas at a high voltage bias, the trap state can suppress the response.[98,99] The Nyquist plots from EIS measurements are shown in Figure 15b. These plots were fitted with an equivalent electrical circuit, which is shown in Figure 15b for analysis. The equivalent electrical circuit included one resistance and two parallel resistance–capacitance (RC) connected in series.[100] R_s is the series resistance, and R_t is the CT resistance. R_{rec} is the

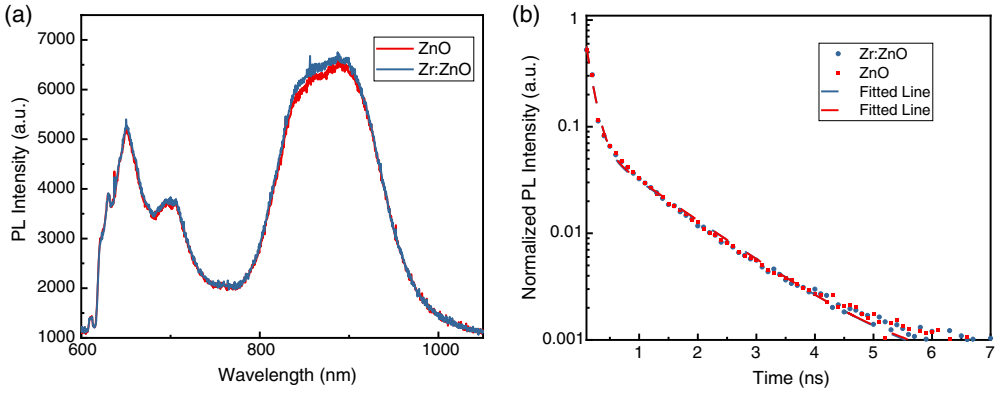

Figure 14. a) Steady-state PL emission spectrum and b) normalized TRPL emission spectrum for active layers on top of ITO/ETL. (under the excitation light at the wavelength of 532 nm).

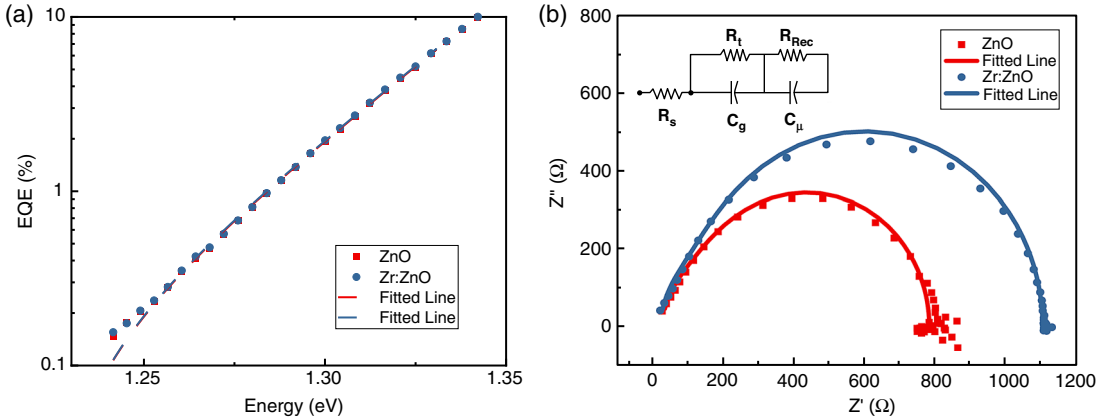

Figure 15. a) EQE spectrum tail versus the incident photo energy and b) Nyquist plots with the equivalent electrical circuit at a bias of 700 mV under the dark condition for both ZnO and Zr:ZnO-based devices.

carrier recombination resistance, which reveals the nonradiative recombination in the device. C_g and C_μ are the dielectric capacitance in the device and the distributed chemical capacitance, respectively.[101–103] **Table 4** lists the obtained electrical parameters from the fitting, including R_s, R_t, R_{rec}, C_g, and C_μ, and the corresponding fitted lines for both types of devices are shown in Figure 15b. From Table 4, it is easy to find that the ALD Zr:ZnO-based device further shows a lower R_s than the control device, which is consistent with the findings in *J*–*V* and dark *J*–*V* measurement. It is worth to mention that the R_s value obtained from EIS measurement is different from the R_s value from *J*–*V* measurement. This is because the current pathway in these two characterization techniques is different, where the direction of current flow is reversed under the dark condition in the EIS test.[7] Moreover, the value of the recombination resistance between the two devices was found very different. By replacing the ZnO with Zr:ZnO, the R_{rec} value has increased by around 48%, which increased from 29.79 to 44.10 Ω cm^2. In the EIS study, the higher the R_{rec} value usually represents a stronger ability to suppress the recombination, thus, indicates lower nonradiative recombination in the device.[7,102] The result reveals that the ALD Zr:ZnO-based device exhibits lower nonradiative recombination than the control device. Thus, the replacement of ZnO with Zr:ZnO can suppress the nonradiative recombination in the device, which can be another reason for the performance enhancement observed. As a different ETL is the only difference between these two types of devices, the suppressed nonradiative recombination can be the surface recombination at the interface between the ETL and active layer. The ALD Zr:ZnO layer apparently provides a more efficient interface between the ETL and active layer than ALD pure ZnO layer.

Table 4. Electronic parameters including R_s, R_t, R_{rec}, C_g, *and* C_μ fitted from the Nyquist plot of both ZnO and Zr:ZnO-based devices at the applied voltage bias of 700 mV under the dark condition.

Devices	R_s [Ω cm^2]	R_t [Ω cm^2]	R_{rec} [Ω cm^2]	C_g [μF cm^{-2}]	C_u [μF cm^{-2}]
ZnO	1.40	29.8	4.11	0.14	0.16
Zr:ZnO	1.17	44.1	4.41	0.14	0.15

Moreover, the photostability of both type of device has been investigated. Both type of as-fabricated devices were put under simulated one-sun light and 85 °C in the ambient air for 5 h degradation and tested with the interval of 1 h. The obtained PCE aging curves were shown in Figure S2, Supporting Information. It was found that there is negligible difference between the ZnO and Zr:ZnO-based devices from the degradation perspective. Both types of devices exhibit a high PCE decrease over 50% after 5 h in air.

Overall, it is found that the better performance of optimized ALD Zr:ZnO-based devices resulted from a lower R_s, higher current extraction possibility, and lower nonradiative recombination when compared with undoped ZnO based devices.

4. Conclusion

In this work, we demonstrated that atomic-scale engineering afforded by ALD could improve ETLs used in OSCs. From the first-principle DFT analysis, we identified that doping ZnO with Zr improves both its optical and electrical properties. Zr-doped ZnO films were subsequently synthesized with ALD, and it was found that a Zr-doping level of 2.4 at% resulted in a significantly increased bandgap and carrier mobility of the film. This layer was subsequently used as an electron transfer layer in the OSCs and was shown to significantly reduce the R_s, improve the interface passivation between the electron transfer and the absorber layer, and improve the current extraction compared with a device with undoped ZnO. This finally resulted in a record efficiency of 14.7% for an inverted solar cell with a PM6:N3 active layer. This work clearly shows the potential of using computational material design in combination with the unique properties afforded by ALD toward achieving the ultimate efficiency limit of OSCs.

Supporting Information

Supporting Information is available from the Wiley Online Library or from the author.

Acknowledgements

G.K.P. and L.D. contributed equally to this work. This work was funded by ARENA as part of ARENA's Research and Development Program—Solar PV Research (Grant 2017/RND007). The computational works were undertaken with the assistance of resources and services from the National Computational Infrastructure (NCI), which is supported by the Australian Government, and through the UNSW-NCI partner trial scheme. The views expressed herein are not necessarily the views of the Australian Government and the Australian Government does not accept the responsibility for any information or advice contained herein. L.D. appreciates the financial support from the Australian Government Research Training Program Scholarship. The authors acknowledge the facilities and the scientific and technical assistance of Dr. Yin Yao at the Electron Microscope Unit (EMU) and of Dr. Bill Bin Gong at the Solid State and Elemental Analysis Unit within the Mark Wainwright Analytical Centre (MWAC) at UNSW. The authors also acknowledge M. Pollard for building micro-photoluminescence (μPL) spectroscopy system, R. Lee Chin for supporting with the μPL experiments, Kean Khoo, and Xin Cui for their assistance with ALD.

Conflict of Interest

The authors declare no conflict of interest.

Keywords

atomic layer deposition, density functional theory calculation, nonfullerene, organic solar cells, zirconium-doped ZnO

Received: May 13, 2020
Revised: June 22, 2020
Published online:

[1] T. Aernouts, P. Vanlaeke, W. Geens, J. Poortmans, P. Heremans, S. Borghs, R. Mertens, R. Andriessen, L. Leenders, *Thin Solid Films* **2004**, *451–452*, 22.
[2] L. Duan, N. K. Elumalai, Y. Zhang, A. Uddin, *Sol, Energy Mater. Sol. Cells* **2019**, *193*, 22.
[3] M. Kaltenbrunner, M. S. White, E. D. Głowacki, T. Sekitani, T. Someya, N. S. Sariciftci, S. Bauer, *Nat, Commun.* **2012**, *3*, 770.
[4] A. Khalil, Z. Ahmed, F. Touati, M. Masmoudi, in *13th Int. Multi-Conference on Systems, Signals & Devices (SSD)*, **2016**, pp. 342–353.
[5] L. Meng, Y. Zhang, X. Wan, C. Li, X. Zhang, Y. Wang, X. Ke, Z. Xiao, L. Ding, R. Xia, H.-L. Yip, Y. Cao, Y. Chen, *Science* **2018**, *361*, 1094.
[6] Z. Xiao, X. Jia, D. Li, S. Wang, X. Geng, F. Liu, J. Chen, S. Yang, T. P. Russell, L. Ding, *Sci. Bull.* **2017**, *62*, 1494.
[7] L. Duan, H. Yi, C. Xu, M. B. Upama, M. A. Mahmud, D. Wang, F. H. Shabab, A. Uddin, *IEEE J. Photovolt.* **2018**, *8*, 1701.
[8] K. Jiang, Q. Wei, J. Y. L. Lai, Z. Peng, H. K. Kim, J. Yuan, L. Ye, H. Ade, Y. Zou, H. Yan, *Joule* **2019**, *3*, 3020.
[9] Y. Lin, B. Adilbekova, Y. Firdaus, E. Yengel, H. Faber, M. Sajjad, X. Zheng, E. Yarali, A. Seitkhan, O. M. Bakr, A. El-Labban, U. Schwingenschlögl, V. Tung, I. McCulloch, F. Laquai, T. D. Anthopoulos, *Adv. Mater.* **2019**, *31*, 1902965.
[10] S. K. Hau, H.-L. Yip, A. K. Y. Jen, *Polym. Rev.* **2010**, *50*, 474.
[11] Z. He, C. Zhong, S. Su, M. Xu, H. Wu, Y. Cao, *Nat. Photon.* **2012**, *6*, 591.
[12] Q. Van Le, J.-Y. Choi, S. Y. Kim, *Flat Chem* **2017**, *2*, 54.
[13] Z. L. Wang, *Chin. Sci. Bull.* **2009**, *54*, 4021.
[14] S. Chaisitsak, T. Sugiyama, A. Yamada, M. Konagai, *Jpn. J. Appl. Phys.* **1999**, *38*, 4989.
[15] A. Soultati, A. Verykios, S. Panagiotakis, K.-K. Armadorou, M. I. Haider, A. Kaltzoglou, C. Drivas, A. Fakharuddin, X. Bao, C. Yang, A. R. B. M. Yusoff, E. K. Evangelou, I. Petsalakis, S. Kennou, P. Falaras, K. Yannakopoulou, G. Pistolis, P. Argitis, M. Vasilopoulou, *ACS Appl. Mater. Interfaces* **2020**, *12*, 21961.
[16] Y. Jiang, L. Sun, F. Jiang, C. Xie, L. Hu, X. Dong, F. Qin, T. Liu, L. Hu, X. Jiang, Y. Zhou, *Mater. Horizons* **2019**, *6*, 1438.
[17] L. Hu, Y. Liu, L. Mao, S. Xiong, L. Sun, N. Zhao, F. Qin, Y. Jiang, Y. Zhou, *J. Mater. Chem. A* **2018**, *6*, 2273.
[18] X. Li, F. Xie, S. Zhang, J. Hou, W. C. H. Choy, *Light: Sci. Appl.* **2015**, *4*, e273.
[19] D. Ouyang, Z. Huang, W. C. H. Choy, *Adv. Funct. Mater.* **2019**, *29*, 1804660.
[20] X. Fan, W. Nie, H. Tsai, N. Wang, H. Huang, Y. Cheng, R. Wen, L. Ma, F. Yan, Y. Xia, *Adv. Sci.* **2019**, *6*, 1900813.
[21] R. K. Ramachandran, C. Detavernier, J. Dendooven, *Nanotechnol. Catal.* **2017**, 335.
[22] X. Meng, *Nanotechnology* **2015**, *26*, 020501.
[23] R. A. Ovanesyan, E. A. Filatova, S. D. Elliott, D. M. Hausmann, D. C. Smith, S. Agarwal, *J. Vacuum Sci. Technol. A* **2019**, *37*, 060904.
[24] Md. Anower Hossain, Khoo Kean Thong, Xin Cui, Geedhika K Poduval, Tian Zhang, Xiang Li, Wei Min Li, B. Hoex, *Nano Mater. Sci.* **2019**, https://doi.org/10.1016/j.nanoms.2019.10.001.
[25] E. Polydorou, M. Botzakaki, C. Drivas, K. Seintis, I. Sakellis, A. Soultati, A. Kaltzoglou, T. Speliotis, M. Fakis, L. C. Palilis, S. Kennou, A. Fakharuddin, L. Schmidt-Mende, D. Davazoglou, P. Falaras, P. Argitis, C. A. Krontiras, S. N. Georga, M. Vasilopoulou, *J. Mater. Chem. C* **2018**, *6*, 8051.
[26] E. Polydorou, M. A. Botzakaki, I. Sakellis, A. Soultati, A. Kaltzoglou, T. A. Papadopoulos, J. Briscoe, C. Drivas, K. Seintis, M. Fakis, L. C. Palilis, S. N. Georga, C. A. Krontiras, S. Kennou, P. Falaras, N. Boukos, D. Davazoglou, P. Argitis, M. Vasilopoulou, *Adv. Mater. Interfaces* **2017**, *4*, 1700231.
[27] M. Vasilopoulou, D. G. Georgiadou, A. Soultati, N. Boukos, S. Gardelis, L. C. Palilis, M. Fakis, G. Skoulatakis, S. Kennou, M. Botzakaki, S. Georga, C. A. Krontiras, F. Auras, D. Fattakhova-Rohlfing, T. Bein, T. A. Papadopoulos, D. Davazoglou, P. Argitis, *Adv. Energy Mater.* **2014**, *4*, 1400214.
[28] J.-C. Wang, W.-T. Weng, M.-Y. Tsai, M.-K. Lee, S.-F. Horng, T.-P. Perng, C.-C. Kei, C.-C. Yu, H.-F. Meng, *J. Mater. Chem.* **2010**, *20*, 862.
[29] P. I. Stakhira, G. L. Pakhomov, V. V. Cherpak, D. Volynyuk, G. Luka, M. Godlewski, E. Guziewicz, Z. Y. Hotra, *Central Eur. J. Phys.* **2010**, *8*, 798.
[30] H. Frankenstein, C. Z. Leng, M. D. Losego, G. L. Frey, *Org. Electron.* **2019**, *64*, 37.
[31] D. Kim, H. Kang, J.-M. Kim, H. Kim, *Appl. Surf. Sci.* **2011**, *257*, 3776.
[32] Ü. Özgür, Y. I. Alivov, C. Liu, A. Teke, M. A. Reshchikov, S. Doğan, V. Avrutin, S. J. Cho, H. Morkoç, *J. Appl. Phys.* **2005**, *98*, 041301.
[33] S. Suwanboon, P. Amornpitoksuk, A. Sukolrat, *Ceram. Int.* **2011**, *37*, 1359.
[34] K.-D. Kim, D. C. Lim, M.-G. Jeong, H. O. Seo, B. Y. Seo, J. Y. Lee, Y. Song, S. Cho, J.-H. Lim, Y. D. Kim, *Bull. Korean Chem. Soc.* **2014**, *35*, 353.
[35] F. Maldonado, A. Stashans, *J. Phys. Chem. Solids* **2010**, *71*, 784.
[36] S. Cornelius, M. Vinnichenko, N. Shevchenko, A. Rogozin, A. Kolitsch, W. Möller, *Appl. Phys. Lett.* **2009**, 94.
[37] C. Moditswe, C. M. Muiva, A. Juma, *Optik* **2016**, *127*, 8317.
[38] P. M. R. Kumar, C. S. Kartha, K. P. Vijayakumar, T. Abe, Y. Kashiwaba, F. Singh, D. K. Avasthi, *Semicond. Sci. Technol.* **2005**, *20*, 120.
[39] A. Hafdallah, F. Yanineb, M. S. Aida, N. Attaf, *J. Alloys Compd.* **2011**, *509*, 7267.

[40] J. Ding, Y. Zhou, G. Dong, M. Liu, D. Yu, F. Liu, *Progr. Photovolt. Res. Appl.* **2018**, *26*, 974.
[41] T. Tsuchiya, T. Emoto, T. Sei, *J. Non-Cryst. Solids* **1994**, *178*, 327.
[42] W. Tang, D. C. Cameron, *Thin Solid Films* **1994**, *238*, 83.
[43] F. Hussain, M. Imran, R. M. A. Khalil, N. A. Niaz, A. M. Rana, M. A. Sattar, M. Ismail, A. Majid, S. Kim, F. Iqbal, M. A. Javid, S. Saeed, A. Sattar, *Phys. E: Low-Dimens. Syst. Nanostruct.* **2020**, *115*, 113658.
[44] T. Zhang, M. A. Hossain, C.-Y. Lee, Y. Zakaria, A. A. Abdallah, B. Hoex, *Appl. Phys. Lett.* **2018**, *113*, 262102.
[45] H. A. Gatz, D. Koushik, J. K. Rath, W. M. M. Kessels, R. E. I. Schropp, *Energy Proc.* **2016**, *92*, 624.
[46] D. Garcia-Alonso, S. E. Potts, C. A. A. Van Helvoirt, M. A. Verheijen, W. M. M. Kessels, *J. Mater. Chem. C* **2015**, *3*, 3095.
[47] R. Baghdad, N. Lemée, G. Lamura, A. Zeinert, N. Hadj-Zoubir, M. Bousmaha, M. A. Bezzerrouk, H. Bouyanfif, B. Allouche, K. Zellama, *Superlattices Microstruct.* **2017**, *104*, 553.
[48] M.-C. Lin, Y.-J. Chang, M.-J. Chen, C.-J. Chu, *J. Electrochem. Soc.* **2011**, *158*, D395.
[49] S. Herodotou, R. Treharne, K. Durose, G. Tatlock, R. Potter, S. Herodotou, R. E. Treharne, K. Durose, G. J. Tatlock, R. J. Potter, *Materials* **2015**, *8*, 7230.
[50] M. Arita, M. Yamaguchi, M. Masuda, *Mater. Transact.* **2004**, *45*, 3180.
[51] F. Wang, X. Zhao, L. Duan, Y. Wang, H. Niu, A. Ali, *J. Alloys Compd.* **2015**, *623*, 290.
[52] X. Cui, K. Sun, J. Huang, C.-Y. Lee, C. Yan, H. Sun, Y. Zhang, F. Liu, M. A. Hossain, Y. Zakaria, L. H. Wong, M. Green, B. Hoex, X. Hao, *Chem. Mater.*, **2018**, *30*, 7860.
[53] M. A. Mamun, H. Baumgart, A. A. Elmustafa, *ECS J. Solid State Sci. Technol.* **2015**, *4*, Q35.
[54] T. Koida, M. Kondo, *Appl. Phys. Lett.* **2006**, *89*, 082104.
[55] M. Morales-Masis, E. Rucavado, R. Monnard, L. Barraud, J. Holovsky, M. Despeisse, M. Boccard, C. Ballif, *IEEE J. Photovolt.* **2018**, *8*, 1202.
[56] B. Subash, B. Krishnakumar, M. Swaminathan, M. Shanthi, *Langmuir* **2013**, *29*, 939.
[57] C. I. Bright, *Soc. Vac. Coaters Bull.* **2007**, 38.
[58] J. P. Perdew, K. Burke, M. Ernzerhof, *Phys. Rev. Lett.* **1996**, *77*, 3865.
[59] H. J. Monkhorst, J. D. Pack, *Phys. Rev. B* **1976**, *13*, 5188.
[60] S. L. Dudarev, G. A. Botton, S. Y. Savrasov, C. J. Humphreys, A. P. Sutton, *Phys. Rev. B* **1998**, *57*, 1505.
[61] X. Zuo, S.-D. Yoon, A. Yang, W.-H. Duan, C. Vittoria, V. G. Harris, *J. Appl. Phys.* **2009**, *105*, 07C508.
[62] M. K. Satheesan, K. Vani, V. Kumar, *Ceram. Int.* **2017**, *43*, 8098.
[63] A. Slassi, N. lakouari, Y. Ziat, Z. Zarhri, A. F. Lamrani, E. K. Hlil, A. Benyoussef, *Solid State Commun.* **2015**, *218*, 45.
[64] L. Shen, R. Q. Wu, H. Pan, G. W. Peng, M. Yang, Z. D. Sha, Y. P. Feng, *Phys. Rev. B* **2008**, 78.
[65] F. Silvearv, A. L. Rosa, S. Lebègue, R. Ahuja, *Phys. E: Low-Dimens. Syst. Nanostruct.* **2012**, *44*, 1095.
[66] P. Yang, Y. Zhao, H. Yang, *Ceram. Int.* **2015**, *41*, 2446.
[67] K. Yim, J. Lee, D. Lee, M. Lee, E. Cho, H. S. Lee, H. H. Nahm, S. Han, *Sci. Rep.* **2017**, *7*, 40907.
[68] L.-N. Bai, J.-S. Lian, W.-T. Zheng, Q. Jiang, *Open Phys.* **2012**, 10.
[69] W. Kern, *J. Electrochem. Soc.* **1990**, *137*, 1887.
[70] D. M. Hausmann, E. Kim, J. Becker, R. G. Gordon, *Chem. Mater.* **2002**, *14*, 4350.
[71] S. Herodotou, R. E. Treharne, K. Durose, G. J. Tatlock, R. J. Potter, *Materials* **2015**, *8*, 7230.
[72] M. A. Mamun, H. Baumgart, A. A. Elmustafa, *ECS Transact.* **2014**, *64*, 205.
[73] J. Tauc, R. Grigorovici, A. Vancu, *Phys. Status Solidi B* **1966**, *15*, 627.
[74] E. Burstein, *Phys. Rev.* **1954**, *93*, 632.
[75] J. F. Moulder, *Phys. Electron.* **1995**, 230.
[76] A. D. Dhass, E. Natarajan, L. Ponnusamy, in *Int. Conf. on Emerging Trends in Electrical Engineering and Energy Management*, Wiley Online Library **2012**, pp. 382–386.
[77] B. Qi, J. Wang, *Phys. Chem. Chem. Phys.* **2013**, *15*, 8972.
[78] M. A. Mahmud, N. K. Elumalai, M. B. Upama, D. Wang, F. Haque, M. Wright, C. Xu, A. Uddin, *Sol. Energy Mater. Sol. Cells* **2017**, *167*, 70.
[79] J. D. Servaites, M. A. Ratner, T. J. Marks, *Energy Environ. Sci.* **2011**, *4*, 4410.
[80] W. Lan, Y. Liu, B. Wu, B. Xu, H. Pu, B. Wei, Y. Peng, W. Tian, F. Zhu, *ACS Appl. Energy Mater.* **2019**, *2*, 7385.
[81] C. M. Proctor, M. Kuik, T.-Q. Nguyen, *Progr. Polym. Sci.* **2013**, *38*, 1941.
[82] Y. Wang, B. Wu, Z. Wu, Z. Lan, Y. Li, M. Zhang, F. Zhu, *J. Phys. Chem. Lett.* **2017**, *8*, 5264.
[83] M. Lenes, M. Morana, C. J. Brabec, P. W. M. Blom, *Adv. Funct. Mater.* **2009**, *19*, 1106.
[84] L. Duan, Y. Zhang, H. Yi, F. Haque, R. Deng, H. Guan, Y. Zou, A. Uddin, *Energy Technol.* **2020**, *8*, 1900924.
[85] S. Holliday, R. S. Ashraf, A. Wadsworth, D. Baran, S. A. Yousaf, C. B. Nielsen, C.-H. Tan, S. D. Dimitrov, Z. Shang, N. Gasparini, M. Alamoudi, F. Laquai, C. J. Brabec, A. Salleo, J. R. Durrant, I. McCulloch, *Nat. Commun.* **2016**, *7*, 11585.
[86] D. Bi, C. Yi, J. Luo, J.-D. Décoppet, F. Zhang, Shaik M. Zakeeruddin, X. Li, A. Hagfeldt, M. Grätzel, *Nat. Energy* **2016**, *1*, 16142.
[87] L. Duan, X. Meng, Y. Zhang, H. Yi, K. Jin, F. Haque, C. Xu, Z. Xiao, L. Ding, A. Uddin, *Mater. Chem. Front.* **2019**, *3*, 1085.
[88] C.-C. Chueh, C.-Y. Liao, F. Zuo, S. T. Williams, P.-W. Liang, A. K. Y. Jen, *J. Mater. Chem. A* **2015**, *3*, 9058.
[89] L. Duan, H. Yi, Y. Zhang, F. Haque, C. Xu, A. Uddin, *Sustain. Energy Fuels* **2019**, *3*, 723.
[90] A. A. Mohapatra, V. Kim, B. Puttaraju, A. Sadhanala, X. Jiao, C. R. McNeill, R. H. Friend, S. Patil, *ACS Appl. Energy Mater.* **2018**, *1*, 4874.
[91] W. Gong, M. A. Faist, N. J. Ekins-Daukes, Z. Xu, D. D. C. Bradley, J. Nelson, T. Kirchartz, *Phys. Rev. B* **2012**, *86*, 024201.
[92] J. Lee, K. Vandewal, S. R. Yost, M. E. Bahlke, L. Goris, M. A. Baldo, J. V. Manca, T. Van Voorhis, *J. Am. Chem. Soc.* **2010**, *132*, 11878.
[93] R. A. Street, K. W. Song, J. E. Northrup, S. Cowan, *Phys. Rev. B* **2011**, *83*, 165207.
[94] N. Jain, N. Chandrasekaran, A. Sadhanala, R. H. Friend, C. R. McNeill, D. Kabra, *J. Mater. Chem. A* **2017**, *5*, 24749.
[95] H. Yao, Y. Cui, R. Yu, B. Gao, H. Zhang, J. Hou, *Angew. Chem. Int. Ed.* **2017**, *56*, 3045.
[96] G. Garcia-Belmonte, A. Guerrero, J. Bisquert, *J. Phys. Chem. Lett.* **2013**, *4*, 877.
[97] F. Haque, M. Wright, M. A. Mahmud, H. Yi, D. Wang, L. Duan, C. Xu, M. B. Upama, A. Uddin, *ACS Omega* **2018**, *3*, 11937.
[98] G. Ji, Y. Wang, Q. Luo, K. Han, M. Xie, L. Zhang, N. Wu, J. Lin, S. Xiao, Y.-Q. Li, L.-Q. Luo, C.-Q. Ma, *ACS Appl. Mater. Interfaces* **2018**, *10*, 943.
[99] H. Yi, D. Wang, M. A. Mahmud, F. Haque, M. B. Upama, C. Xu, L. Duan, A. Uddin, *ACS Appl. Energy Mater.* **2018**, *1*, 6027.
[100] B. Arredondo, B. Romero, G. Del Pozo, M. Sessler, C. Veit, U. Würfel, *Sol. Energy Mater. Sol. Cells* **2014**, *128*, 351.
[101] A. Aprilia, P. Wulandari, V. Suendo Herman, R. Hidayat, A. Fujii, M. Ozaki, *Sol. Energy Mater. Sol. Cells* **2013**, *111*, 181.
[102] B. Arredondo, M. B. Martín-López, B. Romero, R. Vergaz, P. Romero-Gomez, J. Martorell, *Sol. Energy Mater. Sol. Cells* **2016**, *144*, 422.
[103] G. Perrier, R. de Bettignies, S. Berson, N. Lemaître, S. Guillerez, *Sol. Energy Mater. Sol. Cells* **2012**, *101*, 210.